Building a cost-effective mechanochemical Raman system: improved spectral and time resolution for in situ reaction and rheology monitoring

Goran Zgrablić,[a] Ana Senkić,[a] Noa Vidović,[b] Krunoslav Užarević,[c] Davor Čapeta,*[a] Ivana Brekalo*[c] and Mario Rakić[a]

SUPPORTING INFORMATION

[a] *Institute of Physics, Bijenička 46, Zagreb, Croatia. E-mail: dcapeta@phy.hr*
[b] *Department of Physics, Faculty of Science, University of Zagreb, Bijenička 32, Zagreb, Croatia*
[c] *Ruđer Bošković Institute, Bijenička 54, Zagreb, Croatia. E-mail: ibrekalo@irb.hr*

TABLE OF CONTENTS

1. MAIN COMPONENTS, COST AND BUILD DETAILS OF THE MECHANOCHEMICAL RAMAN SYSTEM (MCRS) 4

2. CHARACTERIZATION OF THE EXCITATION LASER SPECTRUM 6

3. CALIBRATION OF THE WAVENUMBER AXIS 7

4. POST-PROCESSING OF THE RAW RAMAN SPECTRA 10

5. SPECTRAL RESOLUTION CHARACTERIZATION 12

5.1. mcRS 12

5.2. Renishaw InVia Raman microscope 15

5.3. Fiber-optics Raman system (BWTek+MayaPro) 16

6. LASER SPOT SIZE IN THE AIR, THE RSP SPOT IMAGE SIZE AND ASSESSMENT OF THE OPTICAL ABERRATION AND DIFFRACTION EFFECTS 18

7. LASER SPOT SIZE AND MAXIMAL POWER DENSITY IN THE JAR 20

8. CALIBRATION OF THE RAMAN INTENSITY AXIS: WAVELENGTH RESPONSE FUNCTION 22

9. THE SAPPHIRE WINDOW JAR AND THE MILL 23

10. SPECTRAL RESOLUTION FUNCTION 24

11. REFLECTIVE GRATING AND ITS PARAMETERS 25

12. RAMAN SIGNAL VERSUS SAMPLE MASS 27

13. BASELINE CORRECTION PROCEDURE 28

14. SAMPLE RHEOLOGY MONITORING 29

15. MECHANOCHEMICAL REACTIONS 30

15.1. General details 30

15.2. Experimental details 30

16. SPECTRA OBTAINED WITH COMMERCIAL RAMAN SPECTROMETER 32

16.1. Imidazole crystal and imidazole in EtOH 32

16.2. Salicylic acid and natural linewidths of its narrow peaks 32

16.3. Low wavenumber Raman spectrum of the moc and the zni products 33

17. VIBRATIONAL SOLVATOCHROMISM OF IMIDAZOLE: CRYSTAL VS SOLVENTS 34

18. REFERENCES 36

1. Main components, cost and build details of the mechanochemical Raman System (mcRS)

Table S1-1 List of main components of the mcRS.

label (Fig. 1)	component & main specifications	manufacturer & part number
L	single longitudinal mode diode laser 633 nm	Ushio SLM-632.8-FS-01
FI	Faraday isolator	Thorlabs IO-3D-633-VLP
BE	variable beam expander 633 nm	Linos 4401-258-000-20
F_L	laser-line filter	Semrock FF01-628/40-25
F_R	entry-level long-pass edge filter	Semrock BLP01-633R-25
L_{OBJ}	objective lens: aspheric, f_{OBJ}=20 mm, NA_{OBJ}= 0.52	Thorlabs AL2520H-B
L_{CPL}	coupling lens: aspheric, f_{CPL}=50 mm, NA_{CPL}= 0.20	Thorlabs AL2550H-B
L_{SLT} L_{CAM}	slit & camera lens: aspheric, f/1.8, f_{SLT}= f_{CAM}=50 mm	Nikon AF-S 50mm
G	reflective diffraction grating: 600 lin/mm, 750 nm blaze wavelength	Thorlabs GR25-0608
CAM	industrial-grade CMOS camera: pixel pitch 3.45 μm	FLIR CM3-U3-31S4M-CS

Lens-based spectrometer. The incident angle θ_i=33.5°, defined as the angle between the incident ray and the grating normal (Fig. S11-1 in SI), is chosen to minimize the footprint of the spectrometer. The spectrometer's Numerical Aperture (NA) is NA_{SP}=0.21 or, in another words, it is an f/2.4 spectrometer (see Section 11 for calculation). As $NA_{CPL} \approx NA_{SP}$ we don't waste RSP as they are all well coupled to the spectrometer.

On the other hand, NA_{CPL}should be close enough to NA_{SP}, as this means there is a good spread of the RSP beam over the diffraction grating. For completeness, in Section 11 we have put derivation of the diffraction angle θ if θ_i is fixed (Eq. S11-4) and calculation of the smallest resolvable wavelength difference of a grating $\Delta\lambda_{gr}$ ≈0.05 nm, or in wavenumbers $\Delta\tilde{\nu}_{gr}$≈1 cm^{-1}. The latter value is the best spectral resolution we can obtain from the mcRS.

The Section 5 of SI will demonstrate that the actual spectral resolution $\Delta\tilde{\nu}_s$, depending on the slit width w and the Raman shift $\tilde{\nu}_R$, is 5 to 13 times larger. This drastic worsening of the spectral resolution (note that a smaller number indicates better spectral resolution) comes from the fact that in most cases the major limiting factors of $\Delta\tilde{\nu}_s$ is not the diffraction grating but the FWHM of the entrance slit image W_i[1].

Table S1-2 Cost of main components of the mcRS.

Component	**Approx. value (EUR)**
Single Longitudinal Mode diode laser	3500
Camera	500
Objective	300
Entry-level Raman edge filter	400
Optical grating	200
Optomechanical components	2000
Optical components	1600
TOTAL	**8500**
ADDITIONAL COMPONENTS	
Low-wavenumber Raman edge filter (25.9 cm^{-1} transition)	900

Table S1-3 Cost of the fiber-optic Raman spectrometers (foRS) employing 785 nm excitation and their technical specifications.

Device	**Technical Specifications**	**Approx. value**	**Quotation date**
Home-made setup: BWTek 102B fiber Raman probe OceanOptics MayaPro2000	Spectral resolution: ~10 cm^{-1} at 1000 cm^{-1}	12,000 €	June 2019
		~15,000 €	December 2024 (Adjusted for inflation)
Commercially available foRS (turn key/plug and play): BWTek i-Raman Plus 785S	Spectral resolution: ~4.5 cm^{-1} at 912 cm^{-1} Spectral range: 65-3350 cm^{-1}	~50,000 €	December 2024
Commercially available foRS (turn key/plug and play): Metrohm Mira XTR Advanced	Spectral resolution: ~8-10 cm^{-1} Spectral range: 400-2300 cm^{-1}	~51,000 €	January 2025

2. Characterization of the excitation laser spectrum

The spectrum of the excitation laser is measured with a Fourier Transform Optical Spectrum Analyzer (FT OSA; Thorlabs OSA201C) set in high-resolution mode and shown in Fig. S2-1. To allow for thermalization of the laser with environment, the spectrum was acquired at least 10 min after switching on the laser.

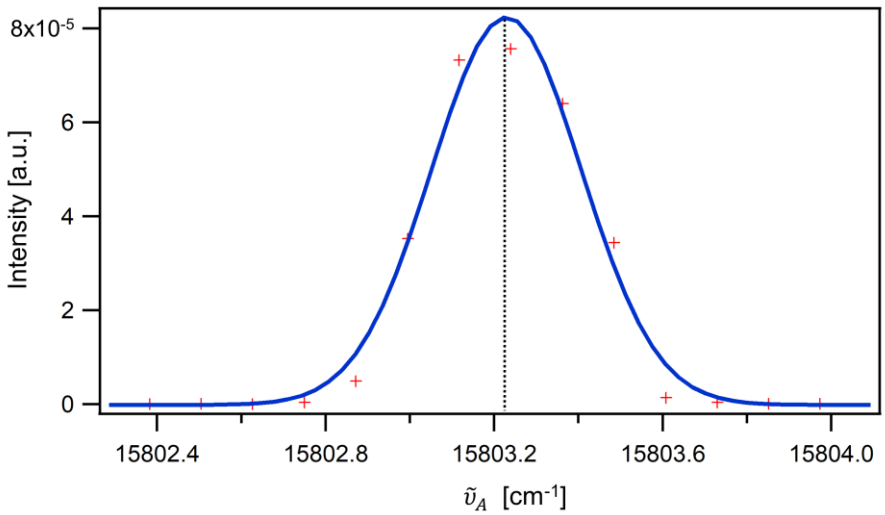

Figure S2-1 Spectrum of the excitation laser (red crosses) acquired with the Fourier Transform Optical Spectrum Analyzer in high resolution mode. The Gaussian fit is shown as blue line.

The spectrum is of Gaussian shape with central wavelength of λ_L=(632.7824±0.0004) nm, or central absolute wavenumber of $\tilde{\upsilon}_L$=(15803.22±0.01) cm^{-1}, and linewidth of $\Delta\tilde{\nu}_L$=(0.4±0.1) cm^{-1}.

However, considering the initial λ_L as a rock-solid value is not possible due to the solid-state lasing mechanism, which lacks the stability of atomic transition-based lasers. Over one month, day-to-day variations of the initial λ_L amounted to ±4 cm^{-1}. Therefore, in the next section (Section 3) we explain the procedure to determine the initial λ_L with uncertainty of ±0.01 nm (±0.25 cm^{-1}) simply by measuring spectra of a Raman shift standard[2] prior to measuring the sample of interest – in this work, cyclohexane was employed as the Raman shift standard. This has additional convenience not only to avoid deployment of FT OSA each day, itself a bulky lab-based device, but also a handy possibility to measure the initial λ_L even in the in-the-field conditions, for example during tandem PXRD/RAMAN in situ monitoring at a synchrotron beamline.

Good news is that once the laser is thermally stabilized—typically after a 10-minute warm-up— λ_L maintains stability within ±0.05 cm^{-1} for eight hours, as claimed by the laser manufacturer. This stability is essential for prolonged milling experiments that may last over an hour.

3. Calibration of the wavenumber axis

Accurate and reproducible Raman spectra enable consistent results across different instruments and under various experimental conditions. Calibration of the wavenumber (Raman shift $\tilde{\upsilon}_R$) axis ensures that minute differences in sample spectra, for example peak shifts of only 2-3 cm^{-1}, reflect actual chemical variations rather than instrumental artifacts. Our calibration protocol involves three key steps and utilizes two reference standards: a neon spectral lamp and cyclohexane (cHex), an ASTM Raman reference standard[7]. These steps include monthly wavelength calibration using the neon lamp, daily laser wavelength measurement with cHex, and daily wavenumber fine-tuning using cHex prior to measuring the sample of interest. The same fine-tuning step is also performed when using the commercial Research Grade Raman System (Renishaw InVia). Together, these steps achieve a measurement uncertainty of less than 1 cm^{-1} for Raman peak positions, ensuring precision across two instruments (mcRS and Renishaw InVia). Details of the calibration procedure are provided in the following.

The first step involves calibrating the spectrometer's wavelength. This procedure is typically needed once per month but becomes essential after significant adjustments, such as realignment of the spectrometer or displacement of the slit. To perform this calibration, a neon spectral lamp (Thorlabs CSL1) is placed at the sample position, providing a reference with 20 atomic emission lines in the 630 – 860 nm range [8]. A quadratic fit is then applied to correlate pixel positions on the detector with corresponding wavelengths (Fig. S3-1). This nonlinear fit is necessary to account for optical field distortions, ensuring that the wavelength axis is accurately mapped.

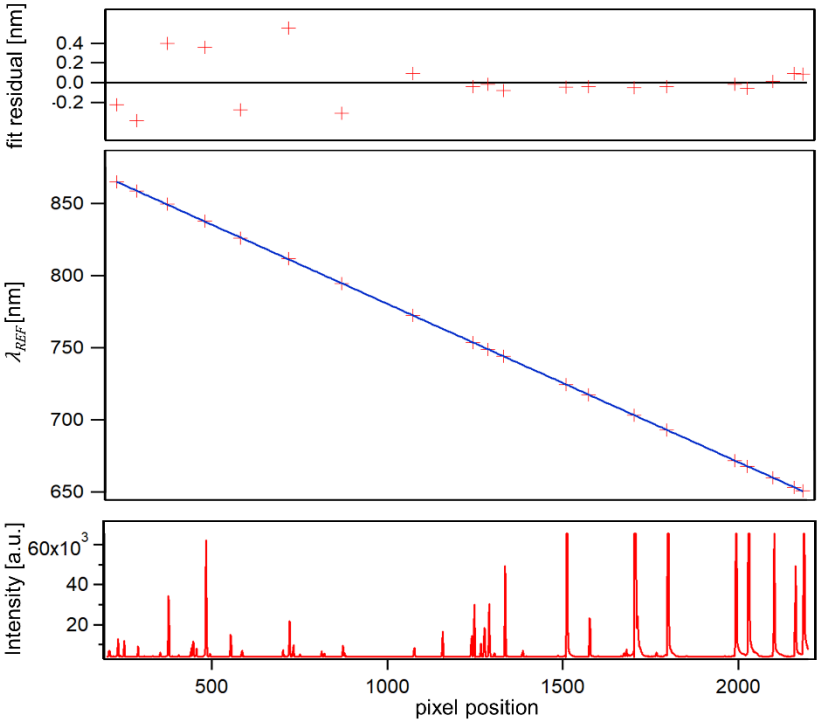

Figure S3-1 Wavelength calibration of the spectrometer with a neon spectral lamp. Middle panel: Pixel position of atomic emission lines versus their reference wavelengths λ_{REF} (red crosses) and a pixel-to-wavelength calibration curve (blue line). The curve is a quadratic fit and the fit residuals are shown in the upper panel. Lower panel: spectrum of the neon spectral lamp at the sample position.

In the next step, we proceed with the measurement of the excitation laser wavelength λ_L. This measurement is crucial as the Raman shift $\tilde{\upsilon}_R$ of a vibrational mode is defined relative to λ_L and it should be conducted each time the laser is turned on, given that solid-state lasers like the one employed in mcRS are susceptible to slight variations due to ambient conditions such as temperature and humidity.

To circumvent the need for daily FT OSA measurements (see Section 2 of SI) —especially impractical for field measurements due to the OSA's bulkiness—we use cyclohexane (cHex) as an ASTM Raman reference standard[7]. The Raman shifts of cHex peaks are known with an uncertainty of less than 1 cm^{-1}.

For a given Raman peak, we plot its absolute wavenumber, $\tilde{\upsilon}_A$, against its reference Raman shift, $\tilde{\upsilon}_R^{ref}$, to determine λ_L through a linear fit (Figure S3-2). For example, one measurement yielded $\tilde{\upsilon}_L$=(15801.1±0.6) cm^{-1}, or λ_L=(632.87±0.02) nm.

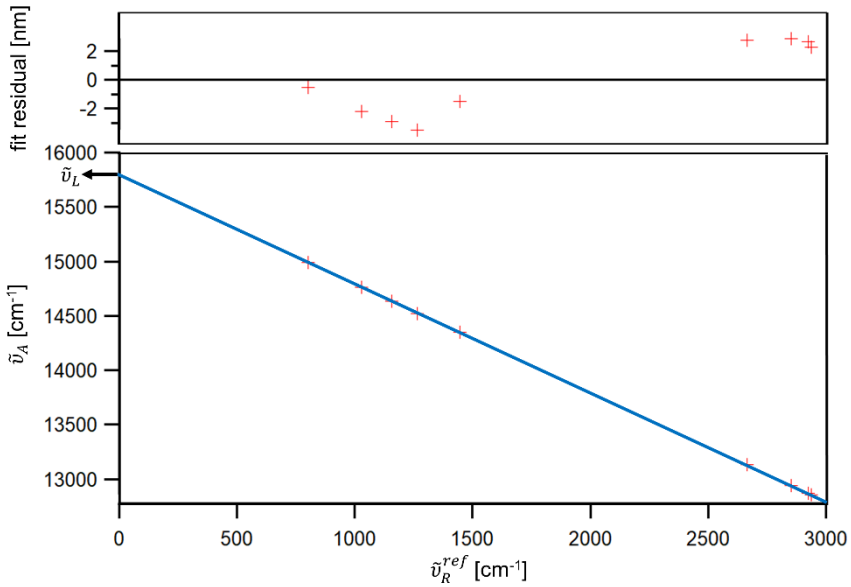

Figure S3-2 Measurement of the excitation laser wavenumber $\tilde{\upsilon}_L$ (wavelength λ_L) with cyclohexane as the reference sample. The absolute wavenumbers $\tilde{\upsilon}_A$ of the reference Raman shifts versus the reference Raman shifts $\tilde{\upsilon}_R^{ref}$ (red crosses) and a linear fit (blue line) to these points. The fit residuals are shown in the upper panel.

The third step of calibration involves fine-tuning of the wavenumber axis, which corrects minor shifts in the spectrometer's wavelength calibration due to ambient temperature variations. This step, also to be performed daily, uses the same cHex measurement from the previous step, now leveraging the known value of $\tilde{\upsilon}_L$ to accurately convert each peak's absolute wavenumber, $\tilde{\upsilon}_A$, into its Raman shift $\tilde{\upsilon}_R$. By calculating the difference, $\Delta\tilde{\upsilon}_{cHex}$, between the measured $\tilde{\upsilon}_R$ and the reference Raman shift $\tilde{\upsilon}_R^{ref}$, we create a correction plot against the reference Raman shift $\tilde{\upsilon}_R^{ref}$ (Fig. S3-3). A quadratic fit accurately describes this relationship, providing a wavenumber fine-tuning function that corrects for any minor discrepancies. This function is then applied to all Raman spectra collected within the subsequent hours, ensuring consistent accuracy.

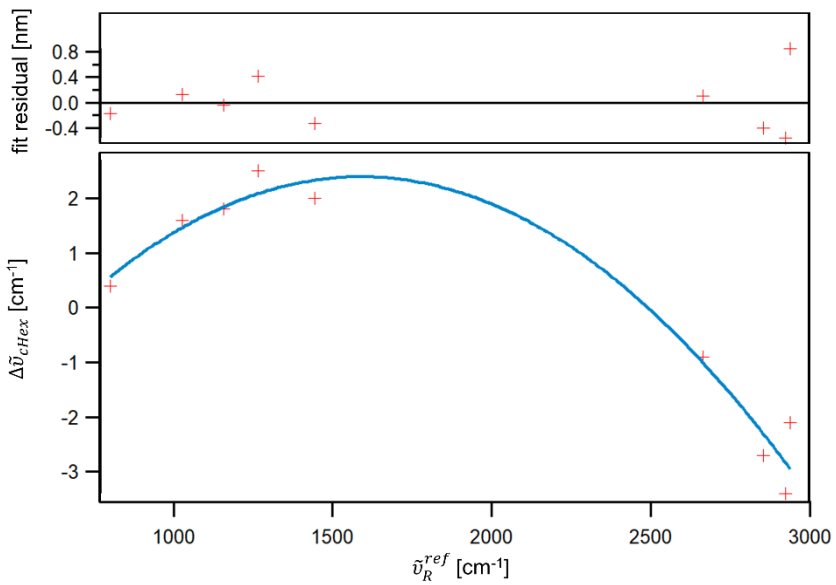

Figure S3-3 Wavenumber fine tuning function (blue line) with cyclohexane as the reference sample. Difference between the measured and the reference Raman shifts $\Delta\tilde{\upsilon}_{cHex}$ versus the reference Raman shifts $\tilde{\upsilon}_R^{ref}$ (red crosses) and a quadratic fit (blue line) to these points. Fit residuals are shown in the upper panel.

4. Post-Processing of the raw Raman spectra

In our experimental approach, we save the entire image rather than just the Raman spectrum that is obtained by column integration along the y-axis (Fig. S4-1). This method provides a dispersed image of the entrance slit.

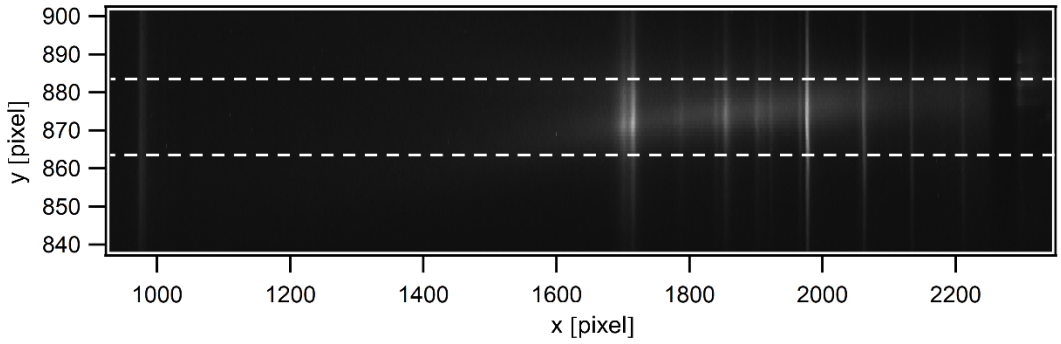

Figure S4-1 From image to the raw Raman spectra. A section of image acquired with the spectrometer's camera when the sample is benzoic acid in the sapphire window jar and the mill is vibrating at 30 Hz. Dashed lines mark the image region that is integrated along the y-axis (20 pixel width) only to become the raw Raman spectrum (Fig. S4-2B).

Before initiating the reaction, we record a spectrum of the empty jar (Fig. S4-2A, red line). This spectrum reveals a broad, featureless band that we refer to as the baseline (dashed line, A and B), along with three distinct Raman peaks from the sapphire window at 379, 417, and 645 cm^{-1}. The baseline likely arises from fluorescence of impurities within the sapphire window, as it weakens when the jar is stationary. In this state, the laser continuously illuminates the same spot, leading to the photobleaching of chromophores associated with these impurities. When the jar resumes motion, the baseline fluorescence recovers.

To correct for this baseline, we developed an automated process based on the Noise Median Method (NMM) introduced by [13] for nuclear magnetic resonance data, which we adapted for mcRS. Details on this adaptation can be found in Section 13 of SI.

After loading the jar with reactants and milling balls, it is repositioned in the vibrating hand, with attention to maintaining a consistent vertical distance from the objective lens. This setup ensures that the focal plane is positioned approximately 0.5 mm above the sapphire window, within the sample cloud. During the milling process, raw Raman spectra are acquired every 2-10 seconds (blue line, Fig. S4-2B). Now in addition to the fluorescence of the window impurities, fluorescence of the sample may add up to the baseline. Due to jar vibrations and the imperfections in the sapphire window, each raw spectrum exhibits slight variations in the baseline (dashed line, Fig. S4-2B), which is subsequently subtracted.

We subtract the baselines of both the empty jar spectrum and the raw sample spectrum. The baseline-corrected empty jar spectrum (red line, Fig. S4-2C) is then normalized to the isolated sapphire peak at 645 cm^{-1} in the baseline-corrected sample spectrum (blue line, Fig. S4-2C). This allows us to obtain a clean Raman spectrum of the sample, corrected for both the baseline and the jar background (Fig. S4-2D).

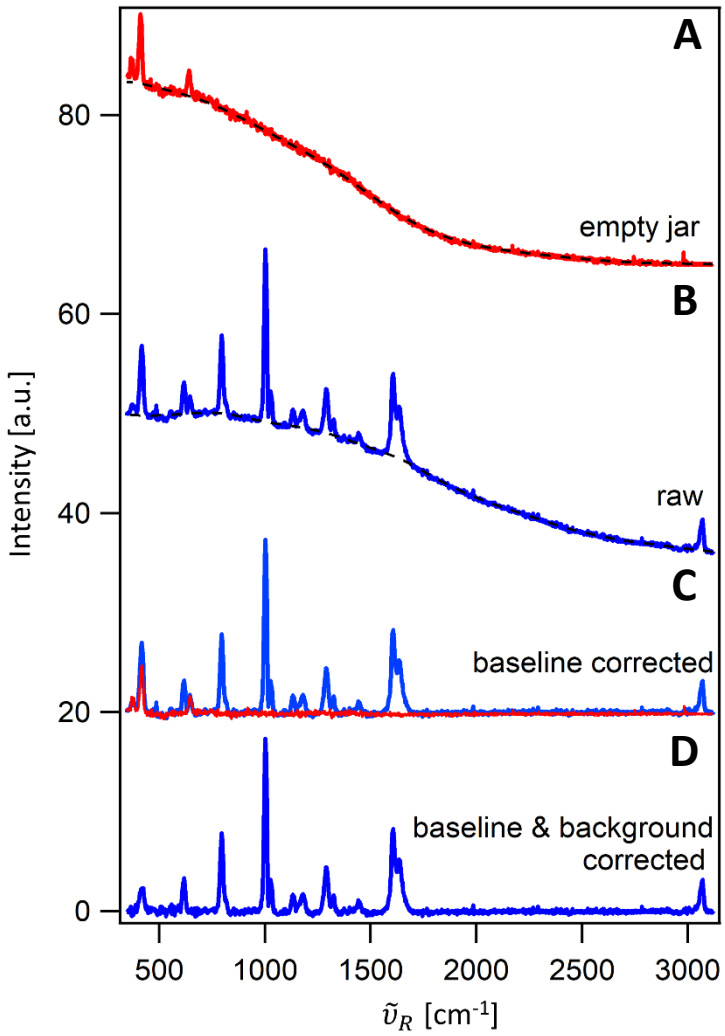

Figure S4-2 Spectra cleanup procedure: from the raw spectra of the empty jar and benzoic acid (A and B, red and blue lines, respectively) to the clean Raman spectrum of benzoic acid (D, blue line). Detailed steps of the cleanup process are described in the main text.

5. Spectral resolution characterization

To characterize the spectral resolution of a spectrometer, we approximate the lineshape of a Raman mode as a Gaussian. The measured linewidth, $\Delta\tilde{\upsilon}_M$, can be described by [1]:

$$\Delta\tilde{\upsilon}_M = \sqrt{\Delta\tilde{\upsilon}_N{}^2 + \Delta\tilde{\upsilon}_L{}^2 + \Delta\tilde{\upsilon}_S{}^2} \qquad \text{(Eq. S5-1)}$$

where $\Delta\tilde{\upsilon}_N$ is the natural linewidth, $\Delta\tilde{\upsilon}_L$ is the laser linewidth, and $\Delta\tilde{\upsilon}_S$ is the spectral resolution of the system.

5.1. mcRS

Given that $\Delta\tilde{\upsilon}_L$ of the SLM 633 nm laser is 0.4 cm^{-1} (Section 2 of SI), more than an order of magnitude smaller than the theoretical $\Delta\tilde{\upsilon}_S$ that can be calculated from Eq. S9-2, the laser linewidth can be neglected. To experimentally determine $\Delta\tilde{\upsilon}_S$, we utilize two reference samples with well-known natural linewidths, measuring $\Delta\tilde{\upsilon}_M$ (i.e. FWHM) of 23 neon emission lines and of two Raman peaks from a calcite crystal. In addition, to mimic the situation during a typical in situ monitoring experiment, $\Delta\tilde{\upsilon}_S$ was also determined by measuring the Raman spectrum of salicylic acid (SA) while 150 mg of the sample was milled at 30 Hz (the same configuration as in Section 15.2 of SI).

The neon lamp, previously used for wavelength calibration, provides very narrow atomic emission lines where $\Delta\tilde{\upsilon}_N << \Delta\tilde{\upsilon}_M$, allowing us to approximate $\Delta\tilde{\upsilon}_S \approx \Delta\tilde{\upsilon}_M$. Positioning of the lamp at the sample position ensures symmetric spectral lines[9] and appropriate detector integration time is chosen to avoid detector saturation.

The calcite sample, obtained from the calibration samples collection at the Institute of Physics in Zagreb, is a stable solid with no absorption bands in the 300-2300 nm range and is resistant to photobleaching. The sample, having a thickness of 0.3 mm, is positioned atop the sapphire window within the jar. Calcite features two sharp peaks with known natural linewidths: $\Delta\tilde{\upsilon}_N$(712 cm^{-1})=2 cm^{-1} and $\Delta\tilde{\upsilon}_N$(1088 cm^{-1})=1 cm^{-1} [10]. We calculate $\Delta\tilde{\upsilon}_S$ for the latter two Raman shifts using:

$$\Delta\tilde{\upsilon}_S \approx \sqrt{\Delta\tilde{\upsilon}_M{}^2 - \Delta\tilde{\upsilon}_N{}^2} \qquad \text{(Eq. S5-2)}$$

For the measurements with SA, we employ three narrow Raman peaks (772, 1030 and 1154 cm^{-1}) whose natural linewidths $\Delta\tilde{\upsilon}_N$ are determined in Section 16.1 and listed in Table S16-1. To mimic the situation during a typical in situ monitoring (Section 15.2 of SI), Raman spectrum was acquired while 150 mg of the sample was milled at 30 Hz, in the sapphire window jar and with two stainless steel balls. Once the FWHM of a Raman peak $\Delta\tilde{\upsilon}_M$ was determined from the Gaussian fit (Fig. S5-2, blue line), $\Delta\tilde{\upsilon}_S$ was calculated from Eq. S5-2. The results are compiled in Table S5-1.

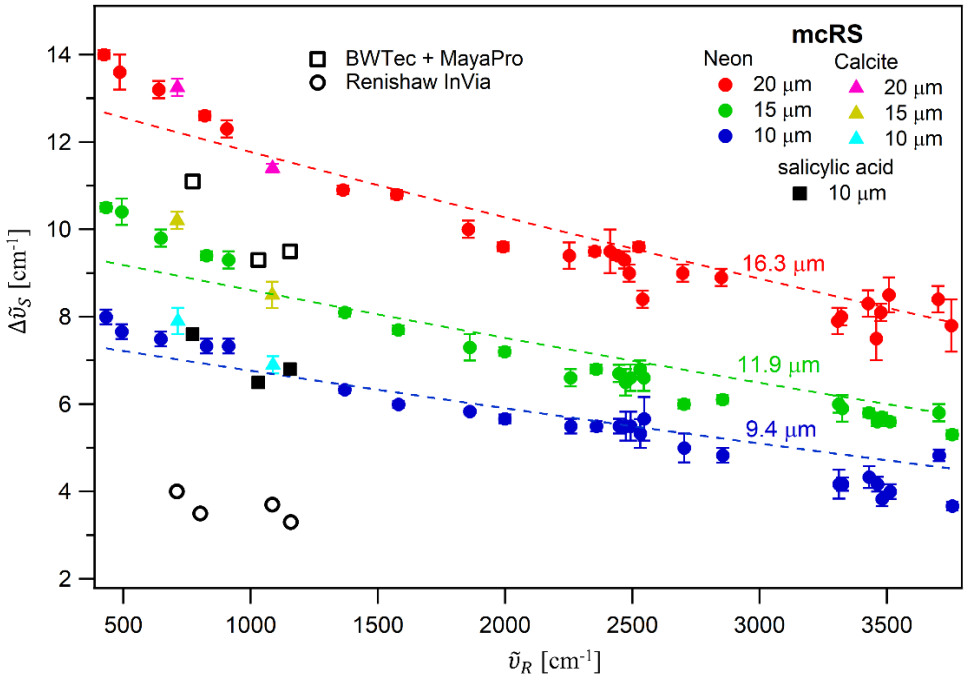

Figure S5-1 Spectral resolution $\Delta\tilde{\nu}_S$ of the mcRS for three slit widths (10, 15, and 20 µm), as determined from the FWHM of neon emission lines (circles), the two Raman peaks of a calcite crystal (triangles) and three Raman peaks of salicylic acid (filled black squares). Measurement of the last sample was performed while it was milled in the jar. The data points are fitted with SRF (dashed lines), and the FWHM of the slit image W_i obtained from the fit are also indicated. For the sake of comparison, $\Delta\tilde{\nu}_S$ of the fiber optics spectrometer (BWTec+MayaPro, empty black squares) and of Renishaw InVia Raman microscope (empty black circles) are included, too.

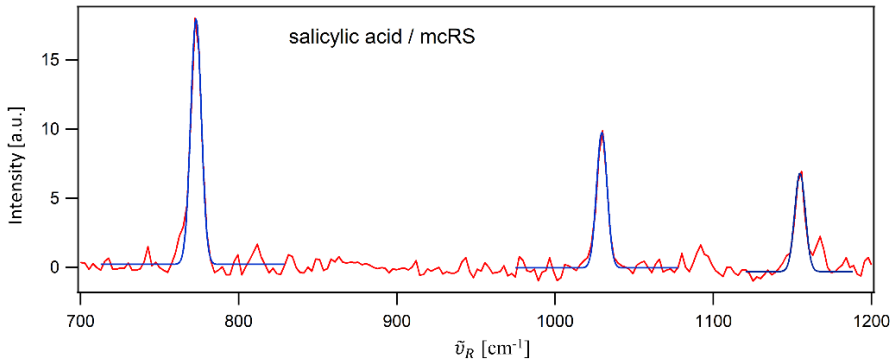

Figure S5-2 Raman spectrum of salicylic acid recorded using the mcRS with a 10 µm slit in place. Only a portion of the spectrum, containing the three narrowest peaks, is shown. The sample was milled at 30 Hz, and Gaussian fits to the peaks are displayed as blue lines.

Table S5-1 Measurement of the spectral resolution $\Delta\tilde{\nu}_S$ of the mcRS with a 10 µm slit in place, determined using the peaks from Fig. S5-2. The measurements were conducted during milling of the sample in the jar.

$\tilde{\nu}_R$ [cm^{-1}]	$\Delta\tilde{\nu}_N$ [cm^{-1}]	$\Delta\tilde{\nu}_M$ [cm^{-1}]	$\Delta\tilde{\nu}_S$ [cm^{-1}]
772	2.2	7.9	7.6
1030	4.1	7.8	6.6
1154	2.9	7.6	7.0

Figure S5-1 compiles all measurements of $\Delta\tilde{\upsilon}_S$ determined using all three samples (neon, calcite, SA). For all slit widths $\Delta\tilde{\upsilon}_S$ obtained from the neon emission lines (red, green and blue circles) and from the calcite Raman peaks (magenta, yellow and turquoise triangles) align well. In addition, $\Delta\tilde{\upsilon}_S$ determined using the SA Raman peaks (filled black squares) also aligns well with the data obtained from neon and calcite and the 10 µm slit in place. It can be concluded that the neon plasma cloud closely resembles the particulate cloud in milling, thus replicating very well the actual experimental conditions.

The experimental data points ($\Delta\tilde{\upsilon}_S$, $\tilde{\nu}_R$) were fitted to the theoretical Spectral Resolution Function (SRF) ([1] and Section 10) described by:

$$\Delta\tilde{\nu}_S(\tilde{\nu}_R) = (\tilde{\nu}_L - \tilde{\nu}_R)^2\, W_i \frac{d}{f_{CAM}} cos\,\theta \qquad \text{(Eq. S5-3)}$$

where all parameters are known, including the laser absolute wavenumber $\tilde{\nu}_L$, the Raman shift $\tilde{\nu}_R$, the grating groove spacing d, the focal length of the camera lens f_{CAM}, and the diffraction angle θ, except for W_i, the FWHM of the slit image. By fitting the data to the SRF, we determined the value of W_i for each slit width w.

The negative slope of SRF, i.e. improved $\Delta\tilde{\upsilon}_S$ at higher $\tilde{\nu}_R$ values, arises from the inherent properties of the wavelength-to-wavenumber (λ-to-$\tilde{\nu}_R$) conversion (Eq. S11-3). In an ideal optical system, where the slit is uniformly illuminated across all wavelengths, all optical aberrations are absent and the spectrometer's magnification M=1, W_i would match w. However, the fitting results reveal that $\Delta\tilde{\upsilon}_S$ is slightly better than what would be expected based on w. Specifically, for the 20 µm and 15 µm slit widths, W_i is approximately 20% smaller than w, while for the 10 µm slit width, it is about 6% smaller. Moreover, an abrupt reduction in W_i of ~0.5 cm^{-1} is seen at $\tilde{\nu}_R$~900 cm^{-1}, a trend that is also observed in the calcite measurements. The latter reduction cannot be attributed to the λ-to-$\tilde{\nu}_R$ conversion and leads us to conclude that W_i is wavelength-dependent.

These observations suggest that the slit is not uniformly illuminated due to the optical system's design. To explore the spread of light reaching the slit, we removed the slit and measured the 1088 cm^{-1} peak of calcite when the crystal is placed in the jar. Under these conditions, the peak exhibited a Lorentzian profile with a FWHM of 13.6 cm^{-1} (Fig. S5-3, dashed line). This setup replicates real experimental conditions, as the calcite Raman source resembles the three-dimensional RSP source, akin to the light distribution during a mechanochemical reaction. Additionally, the calcite peak's narrow linewidth makes it a quasi-monochromatic source suitable for this assessment.

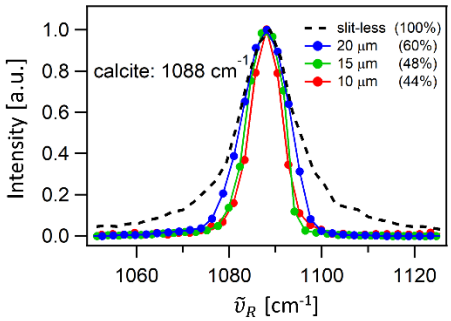

Figure S5-3 The 1088 cm^{-1} Raman peak of calcite crystal acquired with different slit widths w and in the slit-less configuration. All spectra are normalized.

It is important to clarify that the observed Lorentzian is not indicative of a harmonic oscillator, often used in simplified models of Raman-active modes, as in that case the linewidth would be only 1 cm^{-1} [10]. The extended wings observed in the Lorentzian profile point to the contribution of a light cone extending above the focal plane (Fig. S14-1F and H, dashed lines). When the slit is reintroduced and ±10 pixels are integrated along the y-axis it selectively samples the Raman signal primarily from the sample particles situated around the focal plane of the objective lens—approximately those within the optical section defined by the lens's depth of field. This type of Raman signal sampling is usually named as the virtual confocal pinhole[11]. Moreover, the slit truncates the Lorentzian's wings and thus modifies the profile to a Gaussian shape (blue, green, and red lines). By integrating the areas under these bell-shaped curves, we can estimate the photon collection efficiency relative to the slit width. Using the full Lorentzian shape as the baseline for 100% photon capture, we calculated efficiencies of approximately 60%, 48%, and 44% for w of 20 µm, 15 µm, and 10 µm, respectively.

In conclusion, although the 10 µm slit offers approximately twice the spectral resolution of the 20 µm slit, achieving comparable signal-to-noise ratios (SNR) only requires a 35% longer integration time. This demonstrates that the 10 µm slit provides substantial resolution benefits without a prohibitive increase in acquisition time, offering a good balance between resolution and throughput. Thus, all in situ Raman monitoring measurements in this work were taken with the 10 µm slit in place.

5.2. Renishaw InVia Raman microscope

To measure $\Delta\tilde{\upsilon}_S$ of Renishaw InVia Raman microscope, in addition to the Raman peaks of the calcite crystal used in the previous subsection [10], we utilize two narrow Raman peaks of cyclohexane whose natural linewidths $\Delta\tilde{\upsilon}_N$ are also known from the literature[12]. The Raman spectra (Fig. S5-4) were taken with 100x objective (NA = 0.9), while the power on the sample was 1.62 mW. The grating constant was 2400 lines/mm and the acquisition time 5x0.5 s.

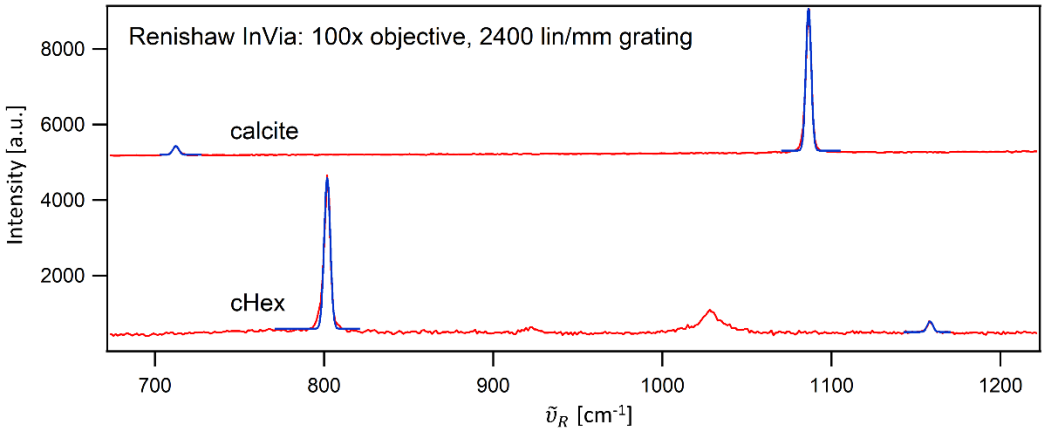

Figure S5-4 Raman spectra of the calcite crystal and cyclohexane taken with Renishaw InVia spectrometer. The calcite spectrum is shifted vertically for clarity and Gaussian fits to the peaks are shown as blue line.

The FWHM of the peaks $\Delta\tilde{\upsilon}_M$ was obtained from the Gaussian fit. Finally, $\Delta\tilde{\upsilon}_S$ was obtained from Eq. S5-2. All parameters are compiled in Table S5-2 while dependence of the spectral resolution on Raman shift is shown on Fig. S5-5.

Table S5-2 Measurement of the spectral resolution $\Delta\tilde{\upsilon}_S$ of Renishaw InVia Raman microscope (100x objective, grating 2400 lines/mm) determined with the calcite crystal and cyclohexane as reference samples.

Reference sample	$\tilde{\nu}_R$ [cm^{-1}]	$\Delta\tilde{\upsilon}_N$ [cm^{-1}]	$\Delta\tilde{\upsilon}_M$ [cm^{-1}]	$\Delta\tilde{\upsilon}_S$ [cm^{-1}]
calcite	714	2	4.5	4.0
cHex	801.2	2.3	4.2	3.5
calcite	1085	1	3.8	3.7
cHex	1157	2.3	4	3.3

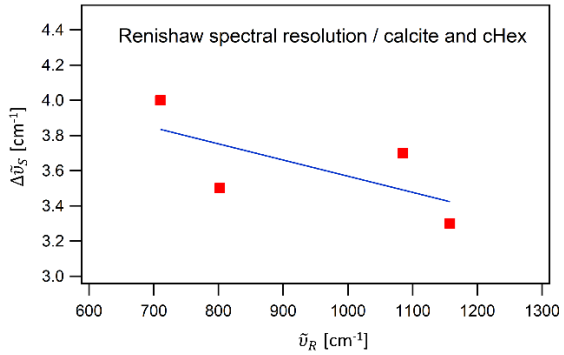

Figure S5-5 The spectral resolution $\Delta\tilde{\upsilon}_S$ of Renishaw InVia Raman Raman microscope determined with calcite and cyclohexane. The linear fit to the data points is also shown (blue line)

5.3. Fiber-optics Raman system (BWTek+MayaPro)

To measure $\Delta\tilde{\upsilon}_S$ of the standard Raman system for in situ monitoring (USHIO SLM 785 nm laser source, BWTek 102B fiber probe, OceanOptics MayaPro2000) we employ three narrow Raman peaks of salicylic acid (772, 1030 and 1154 cm^{-1}) whose natural linewidths $\Delta\tilde{\upsilon}_N$ are determined in Section 16.1 and listed in Table S16-1. To mimic the situation during a typical in situ monitoring (Section 15.2), the Raman spectrum was acquired while 150 mg of the sample was milled at 30 Hz - again in the sapphire window jar and with two stainless steel balls.

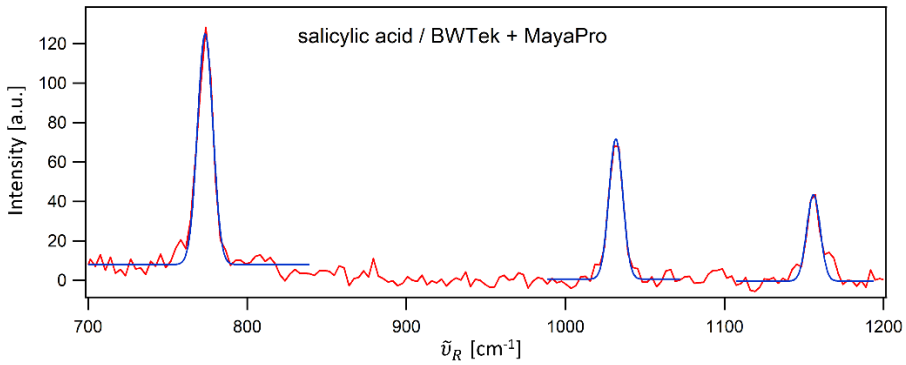

Figure S5-6 Raman spectrum of salicylic acid recorded using with the standard Raman system for in situ monitoring (BWTek+MayaPro) and 15 s integration. Only a portion of the spectrum, containing the three narrowest peaks, is shown. The sample was milled at 30 H, and Gaussian fits to the peaks are displayed as blue lines.

Once the FWHM of a Raman peak $\Delta\tilde{\upsilon}_M$ was determined from the Gaussian fit (Fig. S5-6, blue line), $\Delta\tilde{\upsilon}_S$ was calculated from Eq. S5-2. The results are compiled in Table S5-3.

Table S5-3 Measurement of the spectral resolution $\Delta\tilde{\upsilon}_S$ of the standard Raman system for in situ monitoring (BWTek+MayaPro) by using salicylic acid as the reference sample. The measurement was performed during milling of the sample in the jar.

$\tilde{\nu}_R$ [cm^{-1}]	$\Delta\tilde{\upsilon}_N$ [cm^{-1}]	$\Delta\tilde{\upsilon}_M$ [cm^{-1}]	$\Delta\tilde{\upsilon}_S$ [cm^{-1}]
772	2.2	11.3	11.1
1030	4.1	10.2	9.3
1154	2.9	9.9	9.5

6. Laser spot size in the air, the RSP spot image size and assessment of the optical aberration and diffraction effects

To avoid any ambiguity, in this article the spot size (ex. $2w_0$) is defined as the spot FWHM diameter. The spot 1/e^2 diameter is denoted as $2w_0{}^{1/e^2}$.

First, we characterized the laser spot diameter $2w_0$ when focusing of the laser occurs in the air, i.e. when the sapphire window is absent between L_{OBJ} and the sample (Fig. S6-1D). For this purpose, a beam profiler - an iCMOS camera with a small pixel pitch of 1.85 µm (FLIR BFS-U3-120S4M-CS) - was put in the focus of the objective lens L_{OBJ}. To avoid saturation of the camera, the excitation beam was significantly attenuated with an OD 6 neutral density filter while exposure of the camera was set to 5 ms. The laser spot is of approximately circular Gaussian shape (Fig. S6-1A, B and C) with an average FWHM diameter of $2w_0$=7.5 µm.

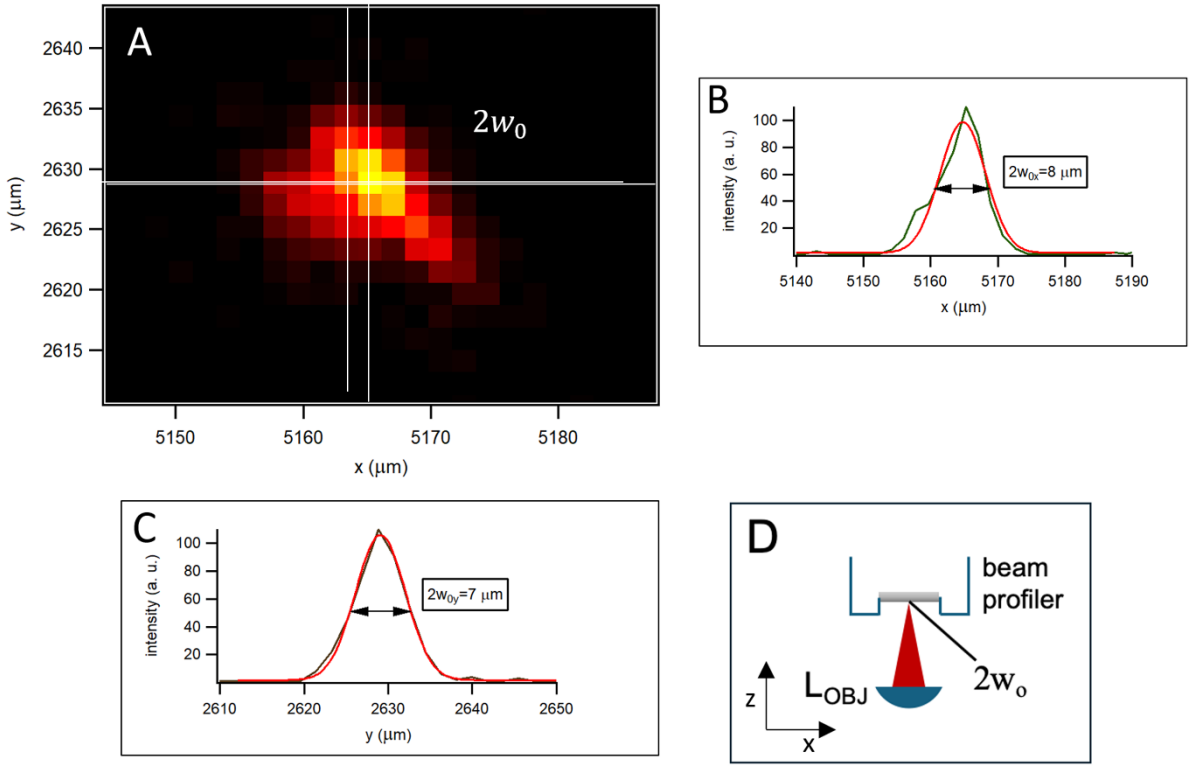

Figure S6-1 A. The laser spot of FWHM diameter $2w_0$ created when the laser beam is refracted only by the objective lens L_{OBJ}. White horizontal and vertical lines mark rows (x-axis or the wavenumber axis) and columns (y-axis, parallel to the entrance slit), respectively, at which the intensity profiles in B and C were acquired; **B.** Intensity profile (1 pixel width) along the x-axis; **C.** As in B but along the y-axis; **D.** Scheme of the setup: the objective lens (L_{OBJ}) focuses the laser beam (red triangle) at the image sensor.

In the next step, a freestanding silicon wafer is put in the same focal plane (i.e. the L_{OBJ} focus). The laser spot creates a Raman Scattered Photons (RSP) spot (Fig. S6-2D) - it is a planar (2D) light source having FWHM diameter of $2w_0$=7.5 µm. Instead of using the Rayleigh scattered photons as signal, for this characterization we opted for the 520 cm^{-1} mode of silicon as signal. In that way we avoided introduction of neutral density filters that would further modify the optical setup.

Then, the L_{CPL} focus is moved along the optical axis (the z-axis), with aid of micrometer driven translation stage, until it arrives at the plane where the entrance slit usually sits (Fig. S6-2D). The focusing is done right when the RSP spot image has the smallest diameter $2w_0'$. We assume that the spectrometer was previously well aligned and thus the foci of L_{SLT} and L_{CAM} are not adjusted. Note that for this characterization the slit is removed from the spectrometer. The spectrometer disperses the image at the slit plane and images it at the camera. Here, the RSP spot image (Fig. S6-2A) is slightly larger along the x-axis ($2w_{0x}'$= 20.5 μm) than along the y-axis ($2w_{0y}'$= 20.1 μm) that stems from the fact that the RSP spot is not monochromatic as the 520 cm^{-1} mode has natural linewidth of Γ[Si]~2.6 cm^{-1} [5,6]. Therefore, we take that the RSP spot image has diameter of $2w_0'$=$2w_{0y}'$=20.1 μm.

The latter number is of great use is it serves as a tool to quantify the optical aberration and diffraction effects [1] introduced by the entire mcRS, i.e. from the sample to the spectrometer's camera. In the absence of the latter effects, in other words considering only the geometrical optics, $2w_0'$ would be 7.5 μm x M_1 x M_2 ~18.8 μm, where M_1=2.5 and M_2=1 are magnifications of the Raman probe and of the spectrometer, respectively. In conclusion, the optical aberration and diffraction effects broaden the RSP image spot by 7%. In the following, we will use this percentage to deduce the laser spot diameter in the jar.

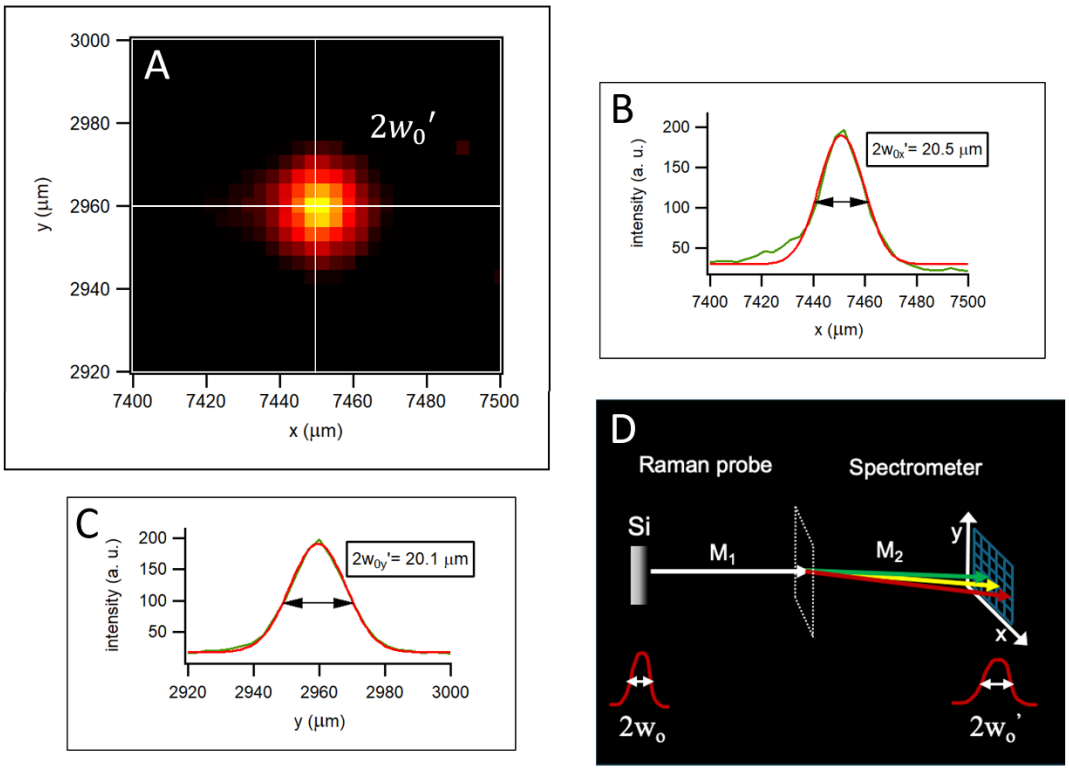

Figure S6-2 A. The RSP spot image, originating from the 520 cm^{-1} mode of a freestanding silicon wafer, acquired with the spectrometer's camera and the entrance slit removed. White horizontal and vertical lines mark rows (x-axis or the wavenumber axis) and columns (y-axis, parallel to the entrance slit) at which the intensity profiles in B and C were acquired; **B.** Intensity profile (1 pixel width) along the x-axis; **C.** As in B but along the y-axis; **D.** Scheme of the imaging process: silicon wafer Si; the FWHM diameter of the RSP spot $2w_0$; white arrow depict imaging of the RSP spot at the plane (dashed rectangle) where the entrance slit usually sits; colored arrows depict dispersion and imaging from the slit plane to the image sensor; magnification of the Raman probe M_1; magnification of the spectrometer M_2; the FWHM diameter of the RSP spot image $2w_0'$.

7. Laser spot size and maximal power density in the jar

To avoid damage of the sample due to photobleaching, it is useful to know the maximal power density (or excitation irradiance) I_S that the sample receives. The sample is usually excited with the laser set at the maximum power when the optical power of P=25 mW is obtained. To calculate I_S we also need to measure the laser spot diameter at the focal plane $2w_J$ when the sample sits in the jar – thus the laser beam now traverses through the sapphire window (Fig. S7-1).

Due to geometrical constraints direct characterization of the laser spot diameter in the jar $2w_J$ (Fig. S7-1D) is not possible. Instead, it is possible to acquire the RSP spot image and measure its FWHM diameter $2w_J'$ (Fig. S7-1A).

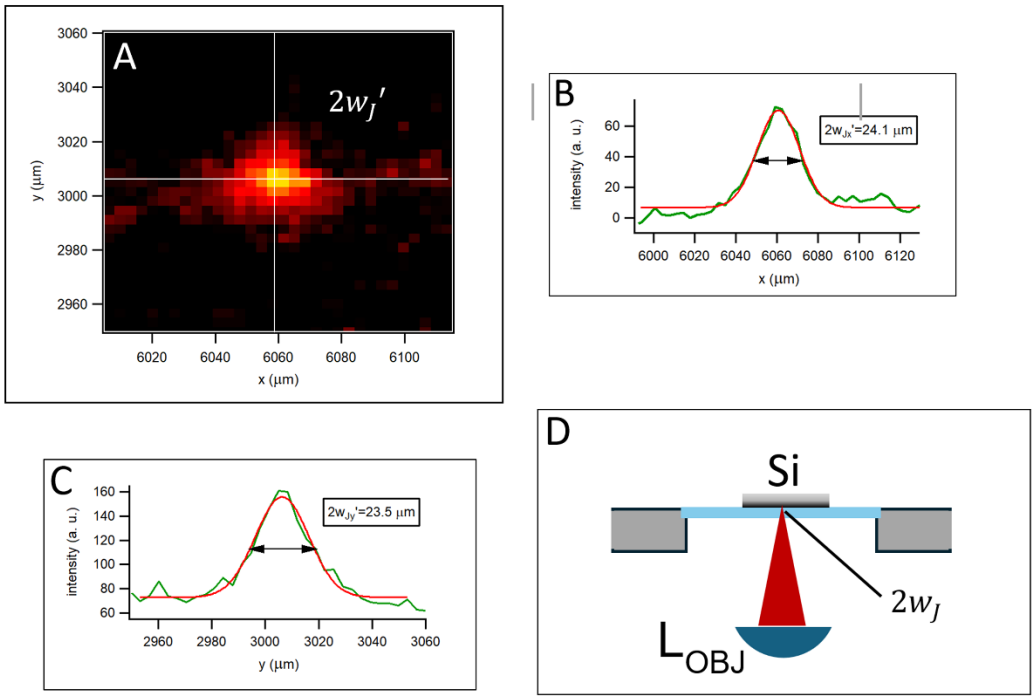

Figure S7-1 A. The RSP spot image, originating from the 520 cm^{-1} mode of a silicon wafer in the jar, placed on the 2 mm thick sapphire window. The latter image is acquired with the spectrometer's camera and the entrance slit removed (slit-free configuration). White horizontal and vertical lines mark rows (x-axis or the wavenumber axis) and columns (y-axis, parallel to the entrance slit) at which the intensity profiles in B and C were acquired; **B.** Intensity profile (1 pixel width) along the x-axis; **C.** Same as in B but along the y-axis; **D.** Scheme of the characterization: silicon wafer Si in the jar; sapphire window – blue line; the laser beam – red triangle; the FWHM diameter of the RSP spot image in the jar $2w_J$.

A piece of silicon wafer is placed inside the jar and placed on the window. The piece is small enough so that it can be in direct contact with the sapphire window. The RSP spot image is of approximately circular Gaussian shape (Fig. S7-1A, B and C): for the same reason explained in Section 5, the RSP spot image is slightly larger along the x-axis ($2w_{Jx}'$= 24.1 µm) than along the y-axis ($2w_{Jy}'$= 23.5 µm). Again, we take that the RSP spot image has diameter of $2w_J'$=$2w_{Jy}'$=23.5 µm. From the latter value, and as we know the broadening induced by optical aberration and diffraction effects (7%) and the total magnification (M=2.5), we can calculate: $2w_J$=23.5/(1.07 x 2.5)=8.8 µm. Finally, it can be concluded that introduction of the sapphire window broadens the laser spot diameter from 7.5 µm to 8.8 µm, or by 17%.

The optical power P at the sample position is measured with a laser power meter (CNI PD100-350T-TP100). When the laser is set at the maximum power, we measure P=25 mW. The power density (excitation irradiance) at focus, i.e. the maximal power density I_S that the sample receives, can now be calculated: $I_S = P/(w_f^2\pi)$=41 kW/cm^2.

8. Calibration of the Raman intensity axis: Wavelength Response Function

With the wavenumber axis calibrated, the next step is to calibrate the Raman intensity axis by determining the Wavelength Response Function (WRF). This step corrects the relative intensities of Raman peaks, ensuring that the ratios between peaks are accurate. To determine WRF, we use a calibrated VIS/NIR light source (Avantes AvaLight-DHS-CAL) coupled to a multimode fiber (Thorlabs M74L02). The fiber has a flat spectral response over the 630-900 nm range, a transmission efficiency exceeding 99.5% and its end is carefully positioned at the sample position to ensure illumination of the slit is as close as possible to the actual experimental conditions.

The WRF is determined by taking the ratio between the known emission spectrum, provided by the light source manufacturer, and the acquired spectrum (Fig. S8-1). In the most useful wavenumber range of 330-3500 cm^{-1}, the WRF remains between 0.8 and 1.4 (Fig. S8-2)., but it increases steeply beyond this range, primarily due to the low quantum efficiency of the silicon based CMOS detector in the NIR region.

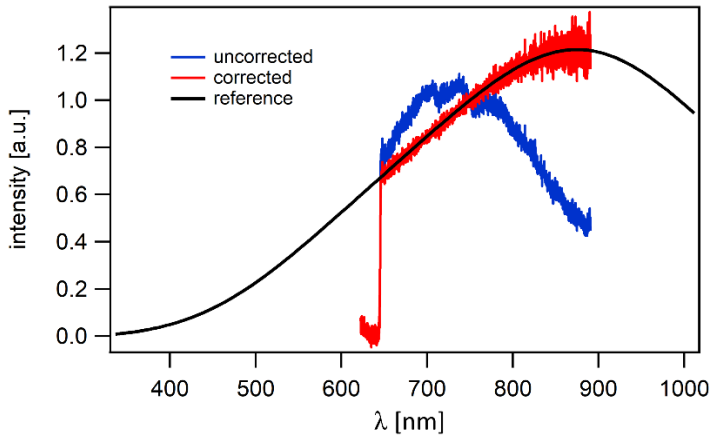

Figure S8-1 Ratio between the known emission spectrum of a wolfram halogen lamp (reference) and the acquired spectrum of the latter lamp (uncorrected) yields WRF (Fig. S8-2). The corrected spectrum of the lamp is also shown (corrected). The spectra are normalized to have unit intensity at 750 nm, the center of mcRS's spectral range.

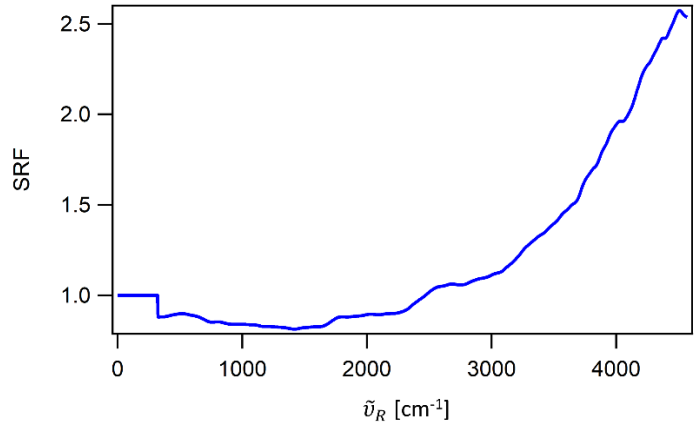

Figure S8-2 WRF of the mcRS (Raman probe and spectrometer together). The lower cutoff frequency is at 330 cm^{-1} (645 nm).

9. The sapphire window jar and the mill

We use a 14 mL aluminum jar based on sapphire windows that was described in our previous work [3]. The jar is mounted in a vibratory ball mill (InSolido Technologies IST-500) operating at 30 Hz. The jar was designed in-house with idea in mind to choose an optical material that has only few isolated Raman peaks in the spectral range covered by mcRS (350-4000 cm^{-1}). In that way, artifacts introduced by subtraction of the jar contribution from the raw Raman spectra will be less prominent and spectrally isolated. Sapphire glass satisfies the last requirement as it shows only two prominent peaks at around 420 and 640 cm^{-1} (easily modelled with a Gaussian which makes their removal from the raw Raman spectra straightforward), whereas PMMA, the most common material from which mechanochemistry jars are made, shows more than 10 peaks in the region covered by the mcRS [4]. In addition, the window employed here is an optical quality glass thus facilitating better collection of Raman Scattered Photons (RSP) from the sample. Finally, sapphire is a highly transparent and extremely hard material that has proved to be able to withstand hour long impacts by stainless steel balls used in the ball-milling process.

10. Spectral Resolution Function

As the basis for derivation of the Spectral Resolution Function (SRF) we use expression for the Raman spectrometer resolution $\Delta\tilde{\nu}_S$ that is based on the FWHM criterion that we will briefly explain in the following: assume a monochromatic light of wavelength λ falls on the entrance slit and that an image of the entrance slit is created on the detector; let's define W_i as the FWHM of the entrance slit image; assume another monochromatic light of wavelength $\lambda + \Delta\lambda_S$ falls on the entrance slit and forms another entrance slit image – then it is considered that two entrance slit images are resolved if they are separated on the detector by a distance W_i, corresponding to the FWHM of the peaks. Based on these assumption Liu and Berg [1] derive the following expression for SRF:

$$\Delta\lambda_S = W_i \frac{d}{f_{CAM}} \cos\theta \qquad \text{(Eq. S10-1)}$$

where W_i is the FWHM of the slit image, d is the grating groove spacing, f_{CAM} is focal length of the camera lens L_{CAM} (Fig. 1A, Table S1-1) and θ is the diffraction angle (Fig. S11-1). The latter parameter is a function of the wavelength or the Raman shift $\theta \equiv \theta(\lambda) = \theta(\tilde{\nu}_R)$, as expressed by Eq. S11-4.

By substituting $\Delta\lambda_S$ into Eq. S11-3, SRF in wavenumbers is obtained:

$$\Delta\tilde{\nu}_S(\tilde{\nu}_R) = (\tilde{\nu}_L - \tilde{\nu}_R)^2 \, W_i \frac{d}{f_{CAM}} cos\,\theta \qquad \text{(Eq. S10-2)}$$

11. Reflective grating and its parameters

For the mcRS device in this article, the following parameters have their values fixed at:

θ_i=33.5°, $\tilde{\nu}_L$=15803.22 cm^{-1} (λ_L=632.78 nm), d=2 µm, m=-1

where θ_i is the incidence angle, $\tilde{\nu}_L$ (λ_L) is the excitation laser wavenumber (wavelength), d is the grating groove spacing (600 lines/mm) and m the diffraction order.

We adopt the convention that if the ray travels from left to right the angle it spans with the grating normal has positive sign. On the other hand, if the ray travels from right to left then the angle has negative sign. In that case the grating equation takes the following form:

$$\sin\theta - \sin\theta_i = \frac{m\,\lambda}{d} \qquad \text{(Eq. S11-1)}$$

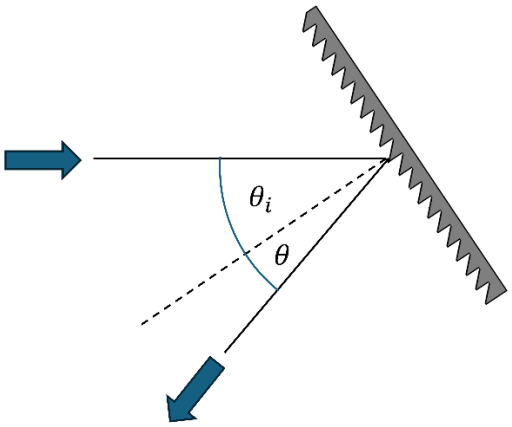

Fig. S11-1 Incident ray impinging on the grating with the incidence angle θ_i and diffracted ray exiting with the diffraction angle θ.

For Raman spectroscopy it is useful to convert wavelengths in wavenumbers. Knowing that the Raman scattered wavelength λ can be described by relation:

$$\lambda = \tilde{\nu}^{-1} = (\tilde{\nu}_L - \tilde{\nu}_R)^{-1} \qquad \text{(Eq. S11-2)}$$

$$\Delta\tilde{\nu}_S = \tilde{\nu}^2\,\Delta\lambda_S = (\tilde{\nu}_L - \tilde{\nu}_R)^2\Delta\lambda_S \qquad \text{(Eq. S11-3)}$$

where $\tilde{\nu}$ is the Raman scattering absolute wavenumber and $\tilde{\nu}_R$ is the Raman shift in wavenumbers, we get diffraction angle θ with $\tilde{\nu}_R$ as the input parameter:

$$\theta(\tilde{\nu}_R) = \arcsin\left[\frac{m}{d\,(\tilde{\nu}_L - \tilde{\nu}_R)} + \sin\theta_i\right] \qquad \text{(Eq. S11-4)}$$

As θ_i is known, it is possible to calculate the smallest resolvable wavelength difference of a grating $\Delta\lambda_{gr}$. The expression for the theoretical resolving power of grating R is:

$$\mathrm{R} = \frac{\lambda}{\Delta\lambda_{gr}} = mN \qquad \text{(Eq. S11-5)}$$

where N is the maximum number of illuminated grooves of the optical grating. In the following we will observe that the grating is entirely illuminated.

As f_{SLT}=50 mm is focal length of the slit lens L_{SLT} and $NA_{CPL} = 0.21$ is NA of the Raman Scattered Photons (RSP) beam propagating from the slit (Fig. 1A), diameter of the beam impinging on the grating D_{SLT} can be calculated from:

$$D_{SLT} = 2\, f_{SLT}\, NA_{CPL} = 21 \text{ mm} \qquad \text{(Eq. S11-6)}$$

However, the grating is square shaped with a side length of l_{gr} =25 mm and is tilted by θ_i (Fig. S11-1). The latter geometry can accept beams whose diameter is not larger than $l_{gr} \cos\theta_i$ =20.8 mm and thus this also limits NA of the spectrometer to NA_{SP} =0.21. As D_{SLT}>20.8 mm we conclude that the entire grating is illuminated with the Raman beam.

Knowing the grating groove spacing d, for diffraction order m=-1 and wavelength corresponding to the central part of a typical Raman spectrum (1600 cm^{-1}/704 nm), from Eq. S11-4 we get $\Delta\lambda_{gr}$:

$$\Delta\lambda_{\mathrm{gr}} = \lambda / N = \lambda\, d / l_{gr} \approx 0.05 \text{ nm} \qquad \text{(Eq. S11-7)}$$

Finally, from Eq. S11-3 we get the smallest resolvable wavenumber difference attainable with the 600 lines/mm grating:

$$\Delta\tilde{\nu}_{gr} \approx 1 \text{ cm}^{-1} \qquad \text{(Eq. S11-8)}$$

12. Raman signal versus sample mass

Optimizing the sample mass in the milling jar is essential for maximizing the Raman signal while avoiding saturation. If too much sample is used, the increased probability of rescattering RSP can lead to signal saturation, as illustrated in Fig. S12-1.

In this work, we apply the mcRS to monitor the reaction between zinc oxide (ZnO) and imidazole (H**Im**). For this characterization we selected H**Im** for the sample due to its significantly larger Raman scattering cross section compared to ZnO. We measured the intensity of two prominent Raman peaks of H**Im** at 1149 cm^{-1} (blue dots) and 1265 cm^{-1} (red dots) as a function of sample mass in the jar (Fig. S8-1 in SI). The signal intensity scales linearly with sample mass up to approximately 150 mg of H**Im** for this reaction, which we determined as the optimal sample mass for this reaction.

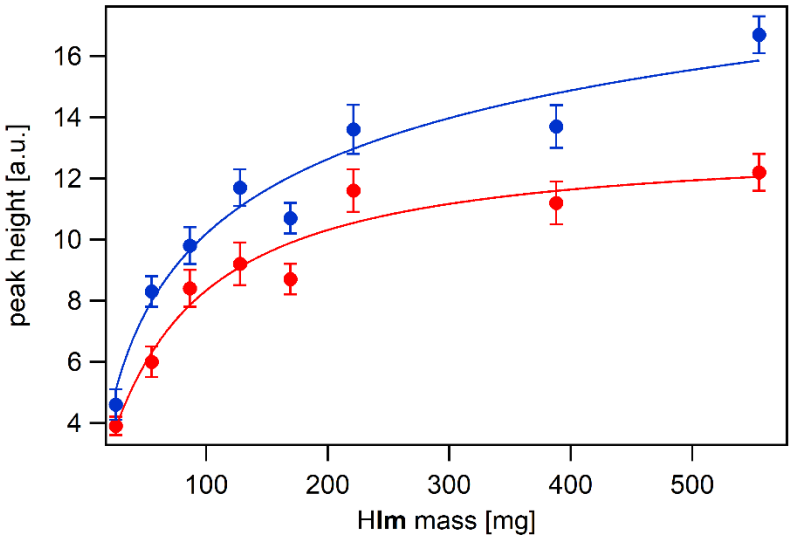

Figure S12-1 Intensity of two prominent Raman peaks of imidazole (1149 cm^{-1} blue, 1265 cm^{-1} red dots) versus mass of the sample in the jar.

13. Baseline correction procedure

The original noise median method (NMM)[13] estimates the baseline at each sampled point by finding the median value of the local minima and maxima within a window of some width W around the sampled point, and then convolving the median values with a normalized Gaussian of some width σ. This method works well if the number of real extrema is negligible compared to the number of extrema that are a product of noise, which is not a good assumption for our dataset.

We therefore introduced another parameter P that is the percentile of extrema taken into consideration when taking the median. For instance, for P=80 only extrema smaller than the 80th percentile extremum count towards the median. This works best in areas where the signal dominates over noise, with real maxima forming about (100-P)% of the total number of extrema within the window. For areas where noise dominates, it biases the estimated baseline slightly downward.

Regarding the points at the spectrum boundaries, the original NMM covers two cases - one where the noise level at one end is about equal to the noise level at the other end (which does not apply in our dataset), and another where the median values for the boundary points (the points within $W/2$ of the spectrum boundaries) are set equal to the value calculated for the point $W/2$ (or N-$W/2$, where N is the total number of points), thereby estimating the baselines as constant for the first and last $W/2$ points. This is a good estimate for data in which $W/2 << N$, but that is not the case for the values of W that proved optimal in our dataset. We instead chose to estimate the baseline around these boundary points such that the value at point number $A < W/2$ is calculated from the window between points number 1 and A+$W/2$, and analogously for points at the higher bound.

14. Sample rheology monitoring

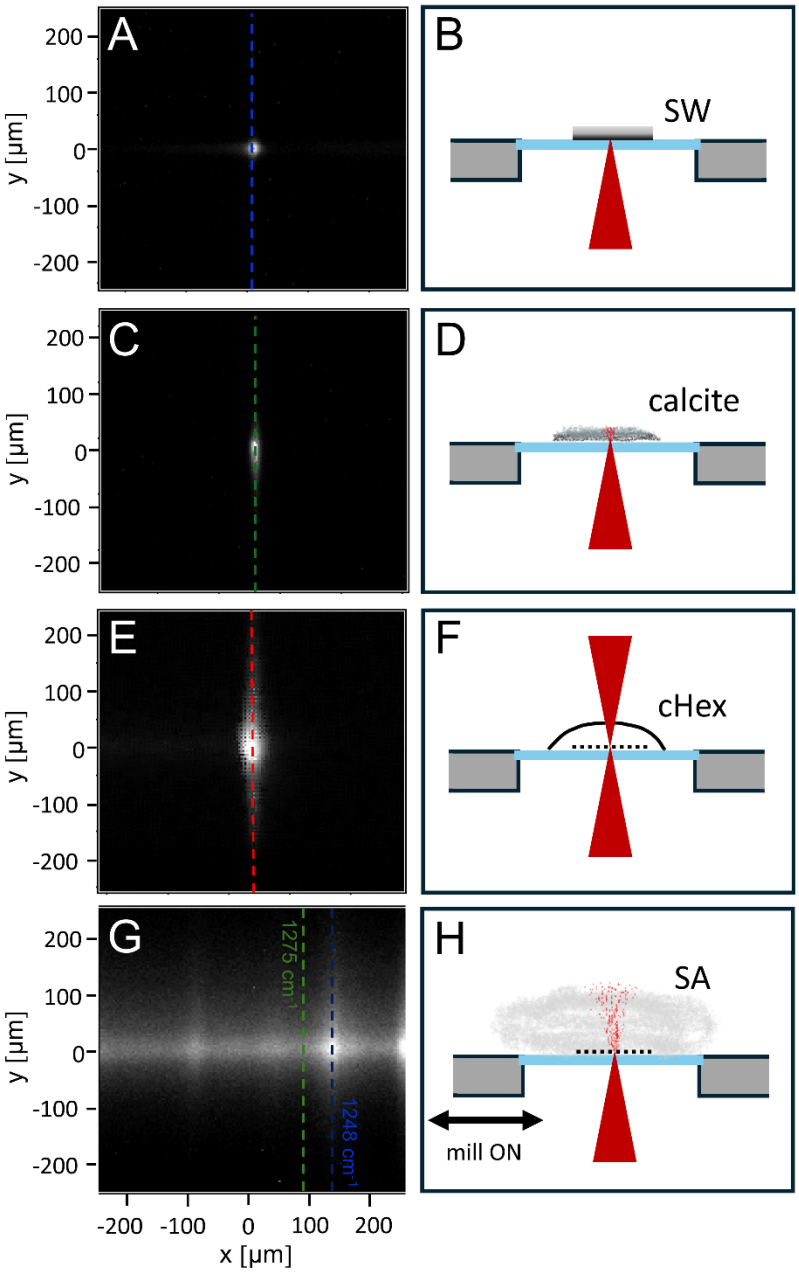

Figure S14-1 A 250x250 µm section of image acquired with the spectrometer's camera when the sample is: **A.** silicon wafer (blue dashed line is at the 520 cm^{-1} mode); **C.** 0.3 mm thick calcite crystal (green dashed line is at the 1088 cm^{-1} mode); **E.** a drop of cyclohexane (red dashed line is at the 801 cm^{-1} mode); **G.** salicylic acid under milling conditions (blue dashed line is at the 1248 cm^{-1} mode, green dashed line sits at the fluorescence signal). The dashed lines are color coded like in Fig. 2 and mark the column along which the y-axis signal in the latter figure is extracted. Schemes: **B.** SW is placed on the 2 mm thick sapphire window (blue line) and brought in the focus of the laser beam (red triangle). The laser spot in the jar has FWHM diameter of $2w_J$; **D.** A 0.3 mm thick calcite crystal is placed on the window; **F.** A drop of cyclohexane is placed on the window and the laser focus is ~0.3-0.5 mm above it (dashed line); **H.** situation when the mill is running and the salicylic acid is turned into a cloud: the laser spot at focus (dashed line) and the excitation conus above coexist. The latter rheology resembles that of a liquid: the central spot becomes less defined, while the surrounding wings increase in intensity, indicative of the more diffused scattering from the suspended particles.

15. Mechanochemical reactions

15.1. General details

Zinc oxide (ZnO) was purchased from Lach-Ner, imidazole (H**Im**) was purchased from Alfa Aesar, ethanol (EtOH) was purchased from Honeywell. All chemicals were used without further purification.

15.2. Experimental details

Powder X-ray diffraction (PXRD) patterns were collected using a Panalytical Aeris powder X-ray diffractometer in the 3-45° 2θ range using a 0.003° step size with an overall scan time of 6 minutes, and Bragg-Brentano geometry, using Cu-Kα radiation (λ=1.5418 Å, 40 kV, 7.5 mA) with the sample mounted on zero background silicon plate.

Analysis of PXRD patterns was conducted using Panalytical X'Pert Highscore Plus[14] software. Experimental patterns were compared to simulated patterns calculated from single crystal structures using Mercury crystal structure viewing software. Crystallographic Information Files containing published crystal structures were obtained from the Cambridge Structural Database (CSD)[15,16].

Milling reactions were conducted in a 14 mL aluminium jar with a sapphire glass window (InSolido Technologies) with one 7 mm (1.4 g) and one 10 mm (4.0 g) stainless steel ball bearing. In a typical experiment, zinc oxide (100.0 mg, 1.23 mmol) and imidazole (167.0 mg, 2.45 mmol) were milled at 30 Hz for 15-90 min using an InSolido Technologies IST-500 mixer mill (corresponding to a Zn:H**Im**=1:2 molar ratio). In the liquid assisted grinding (LAG) reactions, 120 μL (94.8 mg, 2.06 mmol, Zn:EtOH=1:1.7) of ethanol was also added into the milling jar.

In the variable stoichiometry experiments:

a) zinc oxide (75.0 mg, 0.92 mmol) and imidazole (141.2 mg, 2.07 mmol) were milled without liquid to obtain the ZnO-free **moc**-Zn_4**Im**$_8$H**Im** (Zn:H**Im** = 1:2.25)
b) zinc oxide (75.0 mg, 0.92 mmol) and imidazole (125.5 mg, 1.84 mmol) were milled with 100 μL (78.9 mg, 1.713 mmol, Zn:EtOH=1:1.9) of ethanol for a larger EtOH ratio

The products were collected by scraping with a spatula and analyzed without washing or further purification. The reactions were monitored by Raman spectroscopy *in situ*.

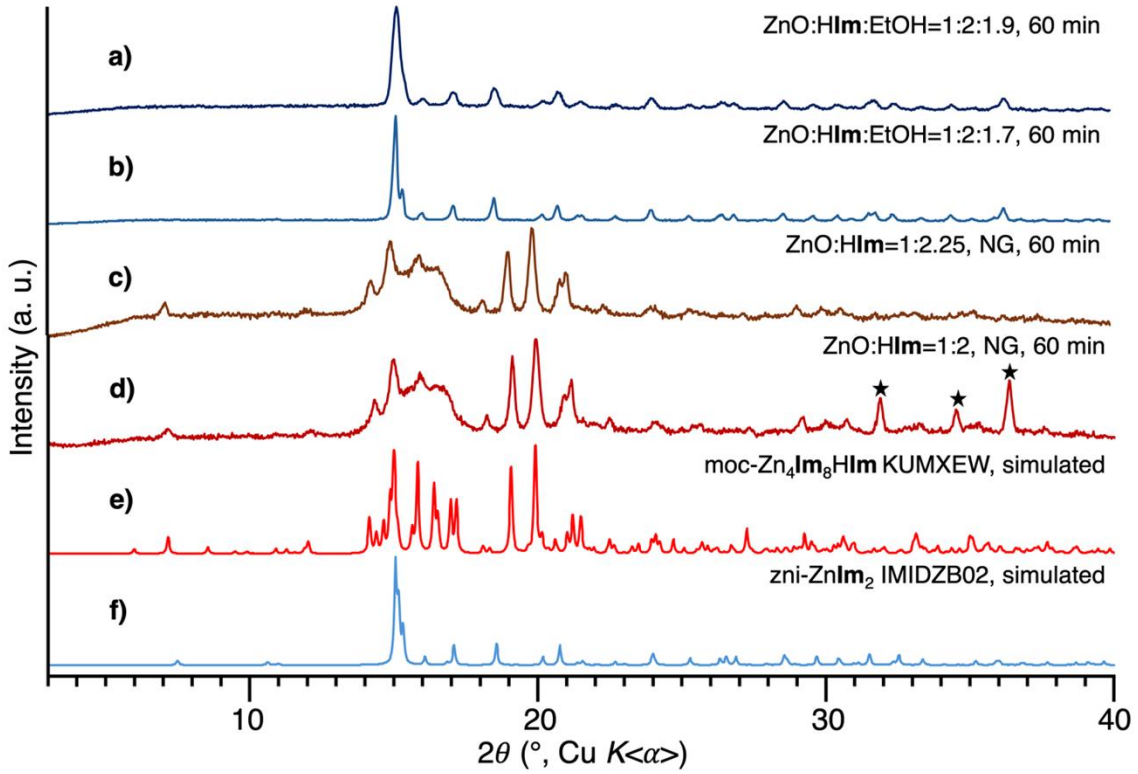

Figure S15-1 PXRD patterns of the products of milling ZnO and H**Im** **a)** with EtOH for 60 min in a Zn:H**Im**:EtOH=1:2:1.9 ratio; **b)** with EtOH for 60 min in a Zn:H**Im**:EtOH=1:2:1.7 ratio; **c)** without added liquid for 60 min in a Zn:H**Im**=1:2.25 ratio; and **d)** without added liquid for 60 min in a Zn:H**Im**=1:2 ratio. Simulated PXRD pattern of **e) moc**-Zn_4**Im**$_8$H**Im** (CSD code KUMXEW); and **f) zni**-Zn**Im**$_2$ (CSD code IMIDZB02). Black stars denote peaks of leftover ZnO reagent.

16. Spectra obtained with commercial Raman spectrometer

Commercial Research Grade Renishaw InVia confocal Raman microscope was used for comparison of overall performance, including spectral resolution and SNR. It is equipped with a 532 nm continuous wave laser source. The spectra were taken with 100x objective (NA = 0.9), while the power on the sample was 1.62 mW. In all the measurements, the grating constant was 2400 lines/mm and the acquisition time 5x0.5 s.

16.1. Imidazole crystal and imidazole in EtOH

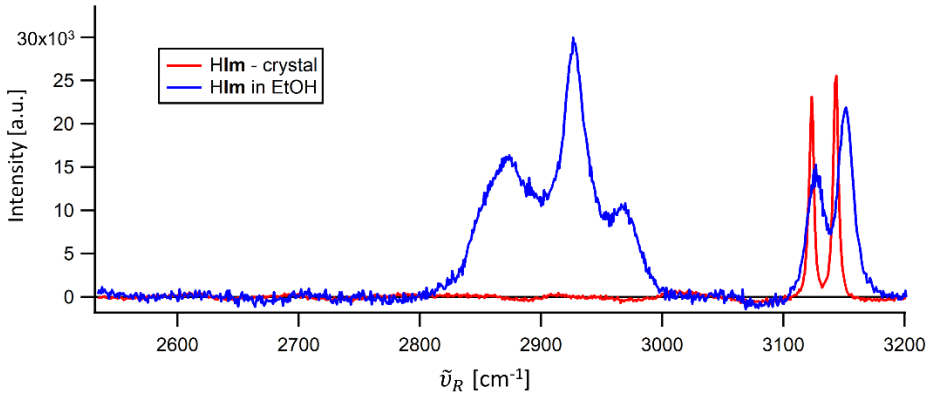

Figure S16-1 Raman spectra of imidazole H**Im** in the high-frequency region: crystal (red line), dissolved in EtOH (blue line). The latter sample has the same concentration as in the LAG reaction (167 mg H**Im** in 100 μL EtOH).

16.2. Salicylic acid and natural linewidths of its narrow peaks

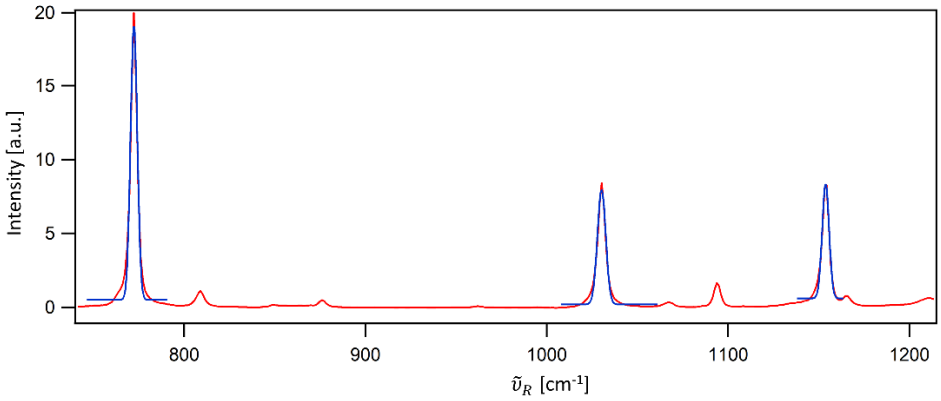

Figure S16-2 Raman spectra of salicylic acid in the region where sit the three narrowest peaks at 772, 1030 and 1154 cm^{-1}. Gaussian fits to the peaks are shown as blue line.

Once the FWHM of a Raman peak $\Delta\tilde{\upsilon}_M$ was determined through the Gaussian fit and the spectral resolution $\Delta\tilde{\upsilon}_S$ was obtained from the linear fit from Fig. S10-4, the natural linewidth $\Delta\tilde{\upsilon}_N$ was calculated from the following expression:

$$\Delta\tilde{\upsilon}_N \approx \sqrt{\Delta\tilde{\upsilon}_M{}^2 - \Delta\tilde{\upsilon}_S{}^2} \qquad \text{(Eq. S16-1)}$$

$\tilde{\nu}_R$ [cm^{-1}]	$\Delta\tilde{\upsilon}_S$ [cm^{-1}]	$\Delta\tilde{\upsilon}_M$ [cm^{-1}]	$\Delta\tilde{\upsilon}_N$ [cm^{-1}]
772	3.8	4.4	2.2
1030	3.5	5.4	4.1
1154	3.4	4.5	2.9

Table S16-1 Determination of the natural linewidths $\Delta\tilde{\upsilon}_N$ of the three narrowest Raman peaks of salicylic acid. $\Delta\tilde{\upsilon}_S$ is the spectral resolution of Renishaw InVia Raman microscope, while $\Delta\tilde{\upsilon}_M$ is the FWHM of the peaks from Fig. S16-2.

16.3. Low wavenumber Raman spectrum of the moc and the zni products

Commercial Research Grade Renishaw InVia confocal Raman microscope can also be used to investigate low wavenumber Raman spectra (< 100 cm^{-1}). In this frequency range, system's collective modes and supramolecular organization can be investigated. To strongly suppress elastic laser scattering (Rayleigh line), a set of 4 volume Bragg gratings were applied. This set of specialized gratings greatly supress the Rayleigh line, making weak low wavenumber Raman modes detectable. The acquisition parameters were: 50x objective (NA = 0.5), 10x1s, 2400 lines/mm grating and 0.73 mW laser power on the sample.

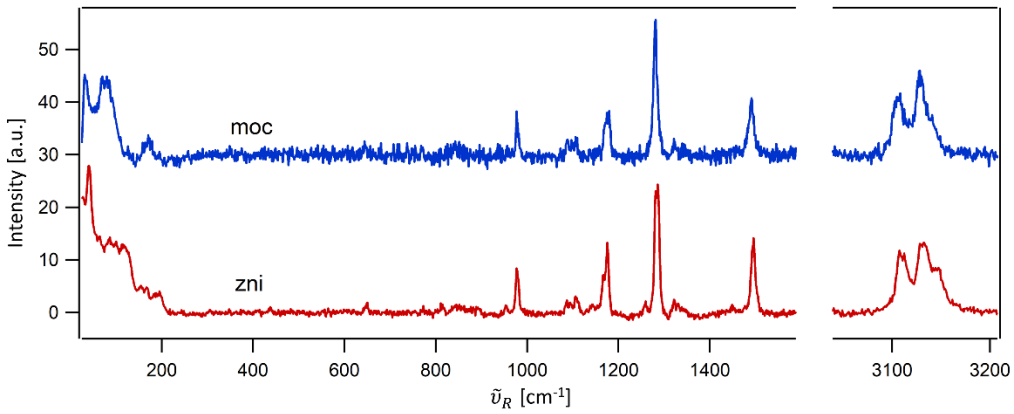

Figure S16-3 Raman spectrum of the products of milling ZnO and H**Im**: **moc**-Zn_4**Im**$_8$H**Im** (blue line) and **zni**-Zn**Im**$_2$ (red line). Note that the spectrum includes the low-wavenumber region (>20 cm^{-1}).

17. Vibrational solvatochromism of imidazole: crystal vs solvents

Raman spectra of the H**Im** crystal, of H**Im** in four solvents with varying polarities and proticities, and of the pure solvents were acquired with the mcRS (Fig. S17-1). The samples, the crystal or a drop of solution, were put on top of a 170 µm thick cover glass. The acquisition parameters were: 1.5 s integration, 25 mW laser power on the sample, 633 nm excitation.

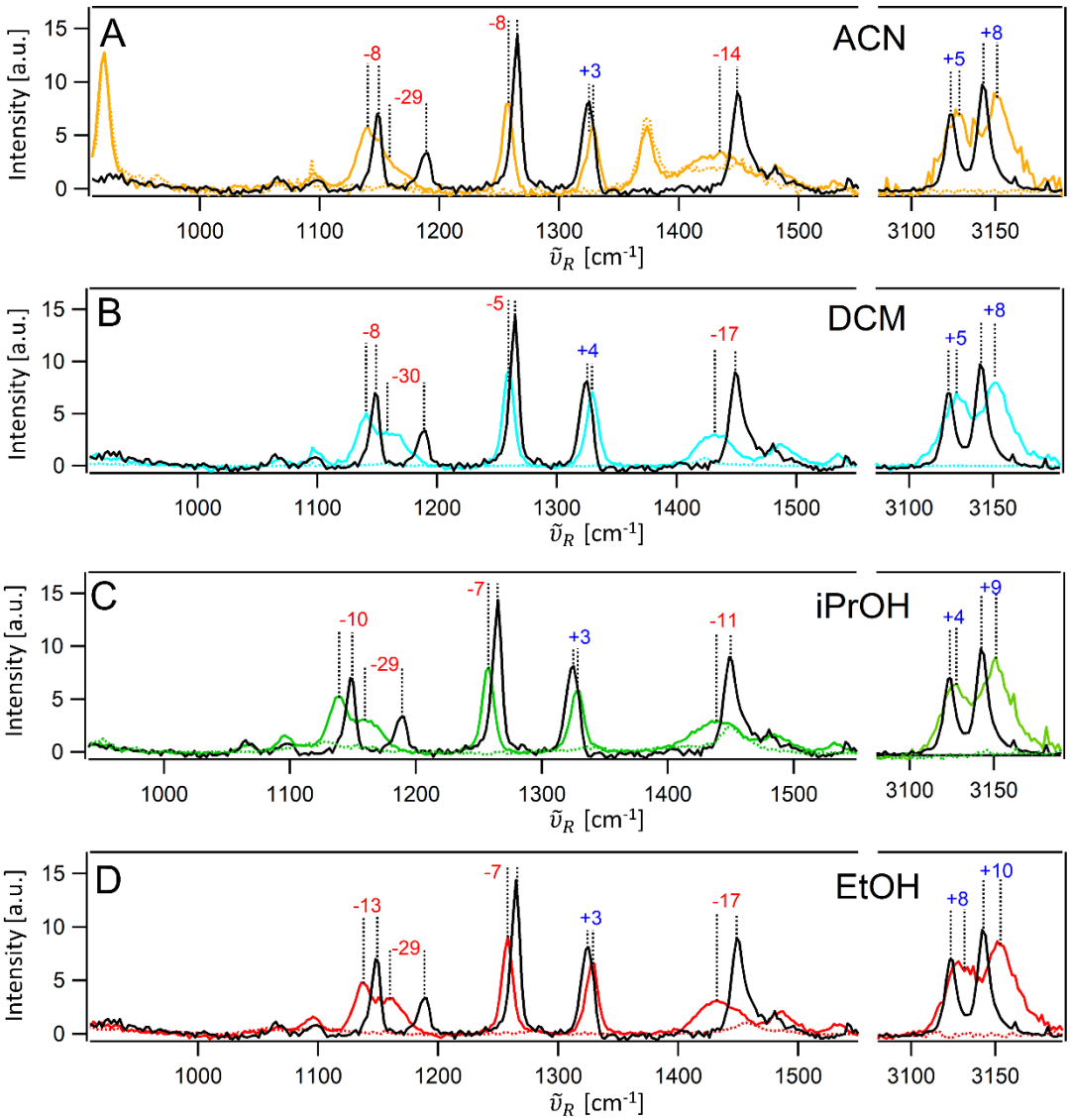

Figure S17-1 Raman spectra of the H**Im** crystal (black line in all panels) and H**Im** in solvents (H**Im**/solv): **A.** acetonitrile (ACN) – yellow line; **B.** dichloromethane (DCM) – turquoise line; **C.** iso-propanol (iPrOH) – green line; and **D.** ethanol (EtOH) – red line. A H**Im**:solvent=1:0.95 ratio was used for all solvents. The spectra of pure solvents are denoted as dashed lines in all panels and were normalized to an isolated solvent peak of the H**Im**/solv samples, i.e. the peak that sits in the spectral range where contribution of H**Im** is absent. The peak shifts in going from the H**Im** crystal to the H**Im**/solv samples are shown above major peaks (red – decrease in frequency, blue – increase in frequency).

Table S17-1 Macroscopic solvent parameters of four solvents used to study vibrational solvatochromism of H**Im**: AN – Gutmann's acceptor number; α – Taft hydrogen bond donating of the solvent; π^* - Taft dipolarity and polarizability scale; and $f(\varepsilon_r, n^2)$ – Onsager's polarity function. For further details see ref. 17.

Solvent	AN	α	π^*	$f(\varepsilon_r, n^2)$	protic
ACN	18.9	0.19	0.75	0.75	-
DCM	20.4	0.13	0.82	0.82	-
iPrOH	33.5	0.76	0.48	0.48	+
EtOH	37.1	0.86	0.54	0.54	+

18. REFERENCES

1 C. Liu and R. W. Berg, *Appl. Spectrosc.*, 2012, **66**, 1034–1043.

2 A. Ntziouni, J. Thomson, I. Xiarchos, X. Li, M. A. Bañares, C. Charitidis, R. Portela and E. Lozano Diz, *Appl. Spectrosc.*, 2022, **76**, 747–772.

3 I. Brekalo, V. Martinez, B. Karadeniz, P. Orešković, D. Drapanauskaite, H. Vriesema, R. Stenekes, M. Etter, I. Dejanović, J. Baltrusaitis and K. Užarević, *ACS Sustain. Chem. Eng.*, 2022, **10**, 6743–6754.

4 S. Lukin, K. Užarević and I. Halasz, *Nat. Protoc.*, 2021, **16**, 3492–3521.

5 C. B. Saltonstall, T. E. Beechem, J. Amatya, J. Floro, P. M. Norris and P. E. Hopkins, *Review of Scientific Instruments*, DOI:10.1063/1.5064804.

6 J. Menéndez and M. Cardona, *Phys. Rev. B*, 1984, **29**, 2051–2059.

7 A. Ntziouni, J. Thomson, I. Xiarchos, X. Li, M. A. Bañares, C. Charitidis, R. Portela and E. Lozano Diz, *Appl. Spectrosc.*, 2022, **76**, 747–772.

8 E. B. Saloman and C. J. Sansonetti, *J. Phys. Chem. Ref. Data.*, 2004, **33**, 1113–1158.

9 C. K. Mann and T. J. Vickers, *Appl. Spectrosc.*, 1999, **53**, 856–861.

10 B. T. Bowie and P. R. Griffiths, *Appl. Spectrosc.*, 2003, **57**, 190–196.

11 N. A. Freebody, A. S. Vaughan and A. M. MacDonald, *Anal. Bioanal. Chem.*, 2010, **396**, 2813–2823.

12 B. N. Toleutaev, T. Tahara and H. Hamaguchi, *Applied Physics B Laser and Optics*, 1994, **59**, 369–375.

13 M. S. Friedrichs, *J. Biomol. NMR*, 1995, **5**, 147–153.

14 M. T. Degen; E. Sadki; U. Bron; G. König and G. Nénert, *Powder Diffr.*, 2014, **29**, S13–S18.

15 K. Yvon, W. Jeitschko and E. Parthé, *J. Appl. Cryst.*, 1977, **10**, 73–74.

16 C. R. Groom, I. J. Bruno, M. P. Lightfoot and S. C. Ward, *Acta Crystallogr. B Struct. Sci. Cryst. Eng. Mater.*, 2016, **72**, 171–179.

17 Y. Marcus, *Chem. Soc. Rev.*, 1993, **22**, 409–416.